



Role of oxygen functionalities on the synthesis of photocatalytically active graphene–TiO₂ composites

Luisa M. Pastrana-Martínez^a, Sergio Morales-Torres^a, Vlassis Likodimos^{b,c}, Polycarpos Falaras^b, José L. Figueiredo^a, Joaquim L. Faria^a, Adrián M.T. Silva^{a,*}

^a LCM - Laboratory of Catalysis and Materials - Associate Laboratory LSRE/LCM, Faculdade de Engenharia, Universidade do Porto, Rua Dr. Roberto Frias, 4200–465 Porto, Portugal

^b Division of Physical Chemistry, Institute of Advanced Materials, Physicochemical Processes, Nanotechnology and Microsystems (IAMPPNM), NCSR Demokritos, 15310 Aghia Paraskevi, Attikis, Athens, Greece

^c Department of Solid State Physics, Faculty of Physics, University of Athens, Panepistimioupolis, GR-157 84 Athens, Greece

ARTICLE INFO

Article history:

Received 24 February 2014

Received in revised form 11 April 2014

Accepted 14 April 2014

Available online 21 April 2014

Keywords:

Graphene oxide

Chemical reduction

Oxygenated surface groups

TiO₂

Photocatalysis

ABSTRACT

Photocatalysis has gained relevance in many applications, including production of fuels, green synthesis of added value products and water detoxification. Graphene–TiO₂ photocatalysts are attracting great attention, but they should be prepared adequately, protecting the carbon material from the surrounding reactive media, maximizing the contact between TiO₂ and graphene, and envisaging broad spectral response. Hereby, graphene oxide was chemically reduced using vitamin C and glucose (environmental friendly reducing agents) as well as hydrazine, and the evolution of the graphene oxygenated surface groups was systematically analyzed (pH_{PZC}, TPD, TG, XPS, DRUV–Vis, Raman and ATR–FTIR). These functionalities (such as epoxy and hydroxyl groups) mediate the efficient and uniform assembly of the TiO₂ nanoparticles on the graphene oxide sheets, leading to highly efficient photocatalysts both under near-UV/Vis and visible light, which is of particular relevance for solar applications.

© 2014 Elsevier B.V. All rights reserved.

1. Introduction

Graphene oxide (GO) has attracted huge interest as a versatile precursor for the synthesis of graphene because oxygen functional groups on the GO surface can be partly removed, resulting in the partial restoration of the *sp*² hybridization and tuning of its electronic properties [1]. Several methods have been proposed to reduce GO, depending on the desired application, including chemical [2], thermal [3], electrochemical [4], photocatalytic [5,6] and/or photothermal reduction [7], among others.

The chemical reduction of GO is a cost-effective and easily scalable method for the production of reduced graphene oxide (rGO) [8]. This methodology can be performed at room temperature or moderately above, with the help of suitable reducing reagents. Since chemical reduction processes rely on chemical reactions, it can be plausibly expected that chemical deoxygenation will be selective to certain groups depending on the reducing reagent. Hydrazine, or hydrazine hydrate, is a well-accepted reducing agent

due to its high reduction efficiency [2,9,10], but it requires considerable care, due to its high toxicity. Therefore, there is an increasing demand to find nontoxic and effective approaches for the chemical production of graphene.

A few successful attempts to develop environment-friendly methods to produce rGO have been already reported, including reducing agents such as vitamin C (L-ascorbic acid) [11,12], glucose [13], L-glutathione [14], green tea [15] and melatonin [16]. rGO obtained by chemical reduction diverges markedly from pristine graphene without defects, since it includes both structural disorder and defects inherited from GO, together with a large amount of residual oxygen functionalities [1,2,10]. Controlled surface chemistry can be used to facilitate the anchoring of semiconductor and metal nanoparticles, or even the assembly of macroscopic structures, which is critical for the efficient utilization of graphene in different applications such as sensors [17,18], supercapacitors [19], batteries [20,21], solar cell and solar fuels [22,23] and, more recently, heterogeneous photocatalysts [24–26].

In the present work, chemical reduction processes using different agents were employed to produce rGO. The ensuing modification of the GO surface chemistry by the partial removal of its functional surface groups has been systematically addressed using different characterization techniques as temperature programmed

* Corresponding author. Tel.: +351 22 0414908.
E-mail address: adrian@fe.up.pt (A.M.T. Silva).

desorption (TPD), Raman spectroscopy, X-ray photoelectron spectroscopy (XPS), thermogravimetry (TG) and attenuated total reflection Fourier transform infrared spectroscopy (ATR–FTIR) for the identification and quantification of the oxygenated surface groups. Despite the high interest in the development of graphene-based photocatalysts as well as their environmental and energy applications [27–39], the role of oxygenated functional groups on the efficiency of GO–TiO₂ composites and heterogeneous photocatalysis has been hardly addressed. These composites have been used for water/wastewater detoxification and disinfection, but mainly for the degradation of dye pollutants, some recent exceptions include a few pharmaceuticals [25,40], endocrine disruptors [41], cyanobacteria and off-odour compounds [42]. In the present work, graphene–TiO₂ composites were prepared using both bare and different chemically reduced GO samples, in order to assess the effect of the nature and amounts of oxygenated groups on the photocatalytic performance of the composite photocatalysts under near-UV/Vis and visible irradiation. Diphenhydramine (2-(diphenylmethoxy)-*N,N*-dimethylethylamine, DP) hydrochloride, an emerging pharmaceutical water pollutant, was used as model contaminant since it is one of the most popular antihistamines and the third most frequently detected pharmaceutical and personal care product (PPCP) in the fillet and liver of fishes collected from five different locations across the United States [43]. The persistence of DP in waters is mainly related to its low biodegradability, also showing high toxicity with mutagenic effects [44].

2. Experimental

2.1. Chemicals

Hydrazine hydrate (50–60%), D-(+)-glucose (99.5%), L-ascorbic acid (99%), ammonium hexafluorotitanate (IV), (NH₄)₂TiF₆ (>99.99%), boric acid, H₃BO₃ (>99%) and high-purity analytical grade DP (99%) were obtained from Sigma-Aldrich.

2.2. Synthesis of graphene oxide

Graphite oxide was obtained by the oxidative treatment of commercial graphite (20 μm, Sigma-Aldrich) following the modified Hummers method as described elsewhere [25,45]. The oxidized material was dispersed in water and sonicated with an ultrasonic processor (UP400S, 24 kHz) for 1 h. The un-exfoliated graphite oxide was removed by centrifugation (20 min at 3000 rpm). Suspensions of GO dispersed in distilled water were obtained and used for the chemical reduction treatments. The load of GO in the suspension was determined by UV–Vis spectrophotometry at 231 nm following a methodology described elsewhere [12].

2.3. Chemical reduction of graphene oxide

rGO samples were synthesized by chemical reduction using vitamin C (rGOV) [12], glucose (rGOG) [13] or hydrazine (rGOH) [9] as reducing agents and employing the aqueous dispersion of GO. During the process, the GO suspension (0.1 g L⁻¹) with the reducing agent (2 mM) was heated at 368 K for 3 h under vigorous stirring. Before reduction, the pH of the GO dispersion was adjusted to 9–10 with 25% ammonia solution to promote the colloidal stability of the GO sheets through electrostatic repulsion.

2.4. Preparation of GO–TiO₂ and rGO–TiO₂ composites

Pristine GO as well as rGO samples (rGOV, rGOG and rGOH) were dispersed in distilled water and sonicated to obtain a homogeneous suspension before the preparation of the respective composite. The composites were synthesized using a dispersion with ammonium

hexafluorotitanate (IV), (NH₄)₂TiF₆ (0.1 mol L⁻¹), and boric acid, H₃BO₃ (0.3 mol L⁻¹), following the liquid phase deposition method (LPD) at room temperature, as described elsewhere [25]. In each run the dispersion was heated at 333 K for 2 h under vigorous stirring with the aim of obtaining a homogeneous suspension. The precipitate was separated by filtration, washed with distilled water and dried at 373 K under vacuum for 2 h without further thermal treatment. During the hydrolysis of (NH₄)₂TiF₆, TiO₂ nanoparticles are gradually produced, interacting with the surface of GO and rGO (e.g., by means of hydrogen bonds) resulting in the formation of GO–T and rGO–T platelets with both sides of graphene sheets covered by TiO₂ nanoparticles [25].

The photocatalysts prepared with GO, rGOV, rGOG and rGOH are labelled as GO–T, rGOV–T, rGOG–T and rGOH–T, where the carbon loading used was ~4 wt.% taking into account the content of GO that leads to the best photocatalytic activity of a composite prepared with TiO₂ and GO for degradation of DP in our previous work [25]. Bare TiO₂ was also prepared by using the same methodology but without addition of any carbon material (Bare–TiO₂). Degussa P25 from Evonik was used as the reference photocatalyst.

2.5. Characterization techniques

UV–Vis absorption spectroscopy measurements were performed by means of a JASCO V-560 UV/Vis spectrophotometer. To obtain the UV–Vis spectra of the powder solids, the spectrophotometer was equipped with an integrating sphere attachment (JASCO ISV-469) and barium sulphate was used as a reference. The reflectance spectra were converted by the instrument software (JASCO) to equivalent absorption Kubelka–Munk units.

The X-ray photoelectron spectroscopy (XPS) analysis was performed with a Kratos AXIS Ultra HSA spectrometer. The analysis was carried out with a monochromatic Al Kα X-ray source (1486.7 eV), operating at 15 kV (90 W), in FAT mode (fixed analyzer transmission), with a pass energy of 40 eV for regions ROI and 80 eV for survey. Data acquisition was performed with a pressure lower than 1 × 10⁻⁶ Pa, and a charge neutralization system was used. Survey and multi-region spectra were recorded at C_{1s}, O_{1s} and N_{1s} photoelectron peaks. For these measurements, the binding energy (BE) values were referred to the C_{1s} peak at 284.9 eV. Each spectral region of photoelectron interest was scanned several times to obtain good signal-to-noise ratios. The spectra obtained after a Shirley background subtraction were fitted to Lorentzian and Gaussian curves using XPS peak 4.1 software.

Thermogravimetric (TG) analysis was performed using a STA 490 PC/4/H Luxx Netzsch thermal analyzer, by heating the sample in air flow from 323 K to 1273 K at 20 K min⁻¹. Attenuated total reflection Fourier transform infrared (ATR–FTIR) spectra were recorded on a NICOLET 510P spectrometer using ZnSe as ATR crystal.

Micro-Raman spectra were measured in backscattering configuration on a Renishaw inVia Reflex microscope using an Ar⁺ ion laser (λ = 514.5 nm) and a high power near infrared (NIR) diode laser (λ = 785 nm) as excitation sources. The laser beam was focused onto the samples by means of a 20× objective, while the laser power density was kept below 0.05 mW μm⁻² to avoid local heating.

Temperature programmed desorption (TPD) analysis was performed in a fully automated AMI-300 Catalyst Characterization Instrument (Altamira Instruments), equipped with a quadrupole mass spectrometer (Dymaxion, Ametek). The carbon sample (0.10 g) was placed in a U-shaped quartz tube inside an electrical furnace and heated at 5 K min⁻¹ up to 1073 K using a constant flow rate of helium (25 cm³ min⁻¹).

The point zero of charge (pH_{pzc}) of the materials was also determined following the methodology described elsewhere [46]. Briefly, solutions with varying initial pH (2–12) were prepared

using HCl (0.1 mol L^{-1}) or NaOH (0.1 mol L^{-1}) and 50 mL of NaCl (0.01 mol L^{-1}) as electrolyte. Each solution was contacted with 0.15 g of the material and the final pH was measured after 24 h of continuous stirring at room temperature. The PZC value of the material was determined by intercepting the obtained final-pH vs. initial-pH curve with the straight line final-pH = initial-pH.

Textural characterization of the materials was obtained from the nitrogen adsorption-desorption isotherms determined at 77 K in Quantachrome NOVA 4200e equipment. Before the analysis, all samples were outgassed for 8 h at 393 K. The apparent surface area (S_{BET}) was determined by applying the Brunauer–Emmett–Teller (BET) equation [47].

2.6. Photocatalytic tests

The photocatalytic activities were evaluated, in a quartz cylindrical reactor filled with 7.5 mL of a 100 mg L^{-1} ($3.40 \times 10^{-4} \text{ mol L}^{-1}$) DP solution, under near-UV/Vis and visible light irradiation. After dark adsorption-desorption equilibrium (60 min), the solution containing the photocatalyst was irradiated with a Heraeus TQ 150 medium-pressure mercury vapour lamp immersed inside a DURAN® glass water cooling jacket that was used to control the operating temperature (298 K) resulting in near-UV/Vis irradiation ($>350 \text{ nm}$, 33 mW cm^{-2}). For visible light, the experiments were performed using a cut-off long pass filter ($>430 \text{ nm}$, 2.8 mW cm^{-2}). In these experiments, the suspension was magnetically stirred and continuously purged with an oxygen flow. The load of catalyst was established in preliminary photocatalytic experiments and, in order to avoid an excess of ineffective catalyst, the load was kept at the optimal value of 1.0 g L^{-1} . Samples taken from the reaction mixture were centrifuged to separate the catalyst particles before analysis. Reaction in the absence of catalyst was performed as a blank experiment in order to characterize direct photolysis.

The concentration of DP was determined by high performance liquid chromatography (HPLC) with a Hitachi Elite LaChrom system equipped with a Hydrosphere C18 column (250 mm \times 4.6 mm; 5 μm particles), a Diode Array Detector (L-2450) and a solvent delivery pump (L-2130). An isocratic method set at a flow rate of 1 mL min^{-1} was used with the eluent consisting of an A:B (70:30) mixture of 20 mM NaH_2PO_4 acidified with H_3PO_4 at pH = 2.80 (A) and acetonitrile (B). The total organic carbon (TOC) was determined using a Shimadzu TOC-5000A analyzer. The maximum relative standard deviation of both HPLC and TOC measurements was never larger than 2%.

3. Results and discussion

3.1. UV–Vis absorption

The UV–Vis absorption spectra of the GO suspension as well as the chemically reduced rGO suspensions (Fig. 1) can be used as a quick probe for the degree of GO reduction. The UV–Vis spectrum of GO exhibits a maximum absorption band at around 231 nm, corresponding to $\pi-\pi^*$ transition of aromatic C=C bonds and a band around 300 nm attributed to $n-\pi^*$ transitions of C=O bonds (typical for GO), in agreement with previous reports [12,48]. After the chemical treatment with different reducing agents (rGOG, rGOV and rGOH), the absorption band at 231 nm presented a red shift to $\sim 260 \text{ nm}$, corresponding to deoxygenation of the GO suspensions by the reduction processes. The reduction of GO is also indicated by the colour change of the solution, i.e. from light brown to black after the reduction process. The black colour observed for the rGO dispersion has been related to the partial restoration of the π network and electronic conjugation [48,49].

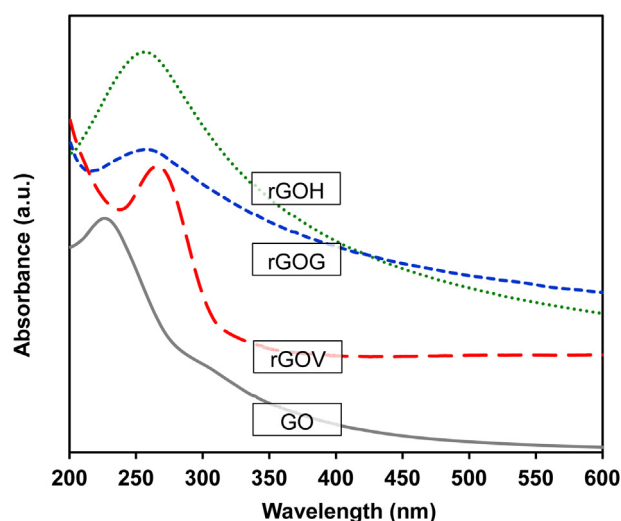


Fig. 1. UV–Vis spectra for GO and reduced samples in water.

3.2. X-ray photoelectron spectroscopy (XPS)

To explore the effect of the different reducing agents on the deoxygenation of GO, XPS measurements were carried out. Figs. S1 a–b, c–d, e–f and g–h (Supporting information) show the deconvoluted C_{1s} and O_{1s} regions of the GO, rGOH, rGOV and rGOG samples, respectively. The binding energies, the corresponding peak areas, the O/C ratios, as well as the oxygen contents (O %), are given in Table 1.

The C_{1s} peak of GO shows the presence of four different types of carbon bonds, as previously observed in literature [50,51]. The binding energy of $\sim 284.6 \text{ eV}$ is attributed to the C=C bonds corresponding to aromatic sp^2 structures, and that of $\sim 285.5 \text{ eV}$ is assigned to C–C (sp^3 carbon species). The binding energy of $\sim 286.4 \text{ eV}$ is typically assigned to C–O, including epoxy (–O–) and hydroxyl (–OH) groups, and the peak at $\sim 287.9 \text{ eV}$ is attributed to C=O, i.e. corresponding to carbonyl (–C=O), carboxyl (–COOH), and carboxylate (–COOR) groups [52]. The oxygen content value was approximately 26.9% and the O/C atomic ratio equal to 0.37, in accordance with the values reported in literature [53]. The results indicate that the major oxygenated species belong to epoxy and hydroxyl groups (24% and 13% for C–O and C=O, respectively).

The high resolution O_{1s} spectrum of GO (Fig. S1b) can be deconvoluted into four components at $\sim 531.3 \text{ eV}$, $\sim 532.4 \text{ eV}$, $\sim 533.3 \text{ eV}$ and $\sim 534.2 \text{ eV}$, corresponding to doubly-bonded oxygen (either in carbonyl or in carboxyl groups), singly-bonded oxygen with two different components assigned to oxygen in alcohol, ether and epoxy groups, and singly-bonded oxygen in carboxyl and ester groups, the last component at higher binding energy corresponding to peroxyacid or peroxyester groups [51]. The results were in agreement with the typical structure of GO, where epoxy and hydroxyl groups located on the basal planes are the major functionalities, whereas carbonyl and carboxyl groups at the edges of GO are minor [1,12,54].

After the chemical reduction, the contribution of the C_{1s} region associated with oxygenated species decreased for all the rGO samples, indicating considerable deoxygenation by the reduction process [9,12]. The intensity of the peak associated to the basal planes groups (C–O, hydroxyl and epoxy) at 286.6 eV decreased significantly, while a slight decrease was observed for the peak at 287.9 eV (C=O) related to groups at the edges of graphene (namely: 24%, 13%, 10% and 11% for C–O, and 13%, 12%, 11% and 12% for C=O, respectively, in GO, rGOH, rGOV and rGOG samples). This agrees with theoretical calculations on the reduction mechanism of GO,

Table 1

Species percentage and corresponding binding energies (in brackets, eV), ratio O/C and oxygen content obtained by XPS analysis.

Sample	O/C	O (%)	C _{1s} (%)				O _{1s} (%)			
			C=C	C–C	C–O	C=O	C=O	C–O (1)	C–O (2)	O=C–OH
GO	0.37	26.9	52(284.6)	11(285.5)	24(286.6)	13(287.9)	14(531.3)	69(532.4)	13(533.3)	4(534.2)
rGOH	0.21	16.7	64(284.6)	11(285.5)	13(286.4)	12(287.9)	25(531.2)	39(532.1)	34(533.2)	2(534.4)
rGOV	0.15	13.4	66(284.6)	13(285.5)	10(286.4)	11(287.9)	27(531.1)	34(532.3)	33(533.4)	6(534.4)
rGOG	0.17	14.5	67(284.6)	10(285.5)	11(286.4)	12(287.9)	27(531.1)	29(532.5)	40(533.4)	4(534.2)

which predict a more difficult removal of oxygen-containing groups located at the edges compared to those located on the basal planes [1,10].

The decrease of hydroxyl and epoxy groups in relation to the carbonyl and carboxyl ones is also visible in the corresponding O_{1s} spectra with the reduction of the peak intensity C–O (1) at the binding energy of 532.4 eV. The degree of deoxygenation of GO by chemical reduction was also observed in the oxygen content of the samples, which yielded values of 26.9%, 16.7%, 13.4% and 14.5% for GO, rGOH, rGOV and rGOG, respectively. Therefore, the lowest O/C ratio for the rGO samples was obtained by treatments performed with glucose and vitamin C (i.e. 0.17 and 0.15, respectively), a better reducing character being observed than that obtained with the toxic hydrazine compound (O/C ratio of 0.21).

The reduction process also leads to a larger intensity of the C=C component after reduction (52% for GO, and 64%, 66% and 67% for rGOH, rGOV and rGOG, respectively), which is indicative of the restoration of the graphitic structure upon reduction, as reported in previous studies [55]. The similar amount of C–C (11%, 11%, 13% and 10% for GO, rGOH, rGOV and rGOG, respectively) is a consequence of the distortion of the carbon lattice during deoxygenation [3].

An additional peak contribution in the deconvoluted C_{1s} spectrum of the rGOH sample indicates the possible presence of C–N bonds, which contribute to the binding energies of C–O bonds and/or C–C bonds [48,55,56]. To better examine this feature, the high resolution N_{1s} region was also deconvoluted (figure not shown) displaying the presence of three types of species, pyridinic N (398.6 eV), pyrrolic N (400.1 eV) and quaternary N (402.5 eV), consistent with previous results in literature [57]. In this case, the most abundant species are both pyrrolic N and quaternary N (41% and 42%, respectively), while pyridinic N occurs at a lower proportion (17%), resulting in a peak area ratio of N/C of about 0.06 for rGOH.

3.3. Thermogravimetric (TG) analysis

The thermal stability of the materials was investigated using TGA analysis. As shown in Fig. 2, the GO sample exhibits a fast weight loss (30 wt.%) at ca. 423–523 K, resulting from the removal of labile oxygenated surface groups, corresponding to the liberation of CO, CO₂ and H₂O. The loss observed above 573 K can be ascribed to desorption of more stable oxygen functional groups in GO [25,58].

The chemical reduction treatments with the different reducing agents seem to increase the thermal stability of the materials regarding the removal of the most labile oxygenated functionalities. In particular, both vitamin C and hydrazine appear to be more efficient in removing the oxygen functionalities than glucose. For the case of rGOG, the weight loss observed at lower temperature could be attributed to remnants of glucose that could not be completely washed away [59].

Nevertheless, all the reduced materials exhibited a mass loss above 573 K indicating that the most stable functionalities can only be partially eliminated after the chemical reduction process, as reported elsewhere [2]. The final sharp mass loss around 750–823 K observed for both GO and rGO corresponds to carbon combustion.

3.4. Attenuated total reflection Fourier transform infrared (ATR-FTIR) spectra

The ATR-FTIR spectra of GO and rGO samples are shown in Fig. 3. The GO spectrum shows typical bands associated with different oxygenated surface groups [55,60]. The broad band at 3000–3500 cm^{−1} is assigned to the vibration of C–OH groups. The absorption band at 1720 cm^{−1} is attributed to carbonyl groups, C=O. The band at around 1300–1370 cm^{−1} corresponds to C–OH stretching. The band at 1220 cm^{−1} corresponds to breathing vibrations of epoxy groups (–O–) and the band at 1050 cm^{−1} is attributed to the stretching vibration of C–O groups (vibrations

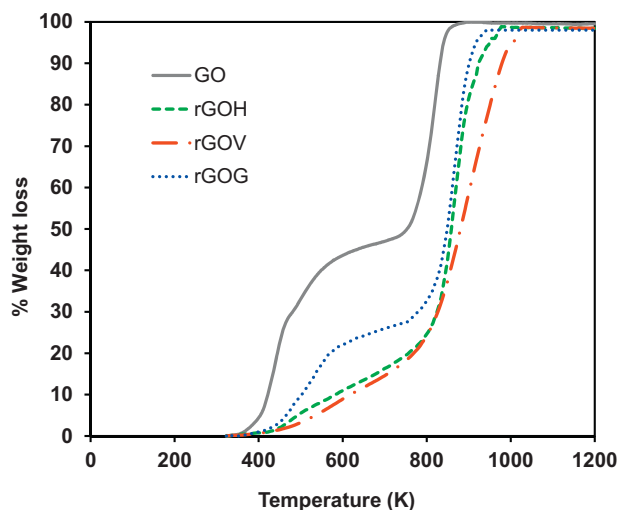


Fig. 2. Thermogravimetric analysis (TG) of GO and reduced samples.

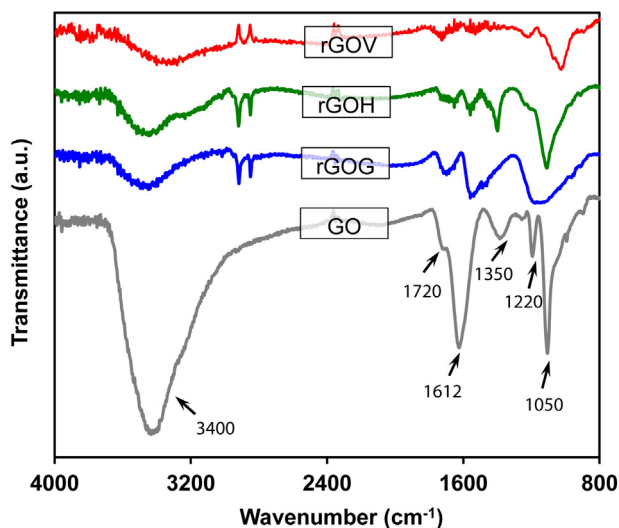


Fig. 3. ATR-FTIR spectra of GO and reduced samples.

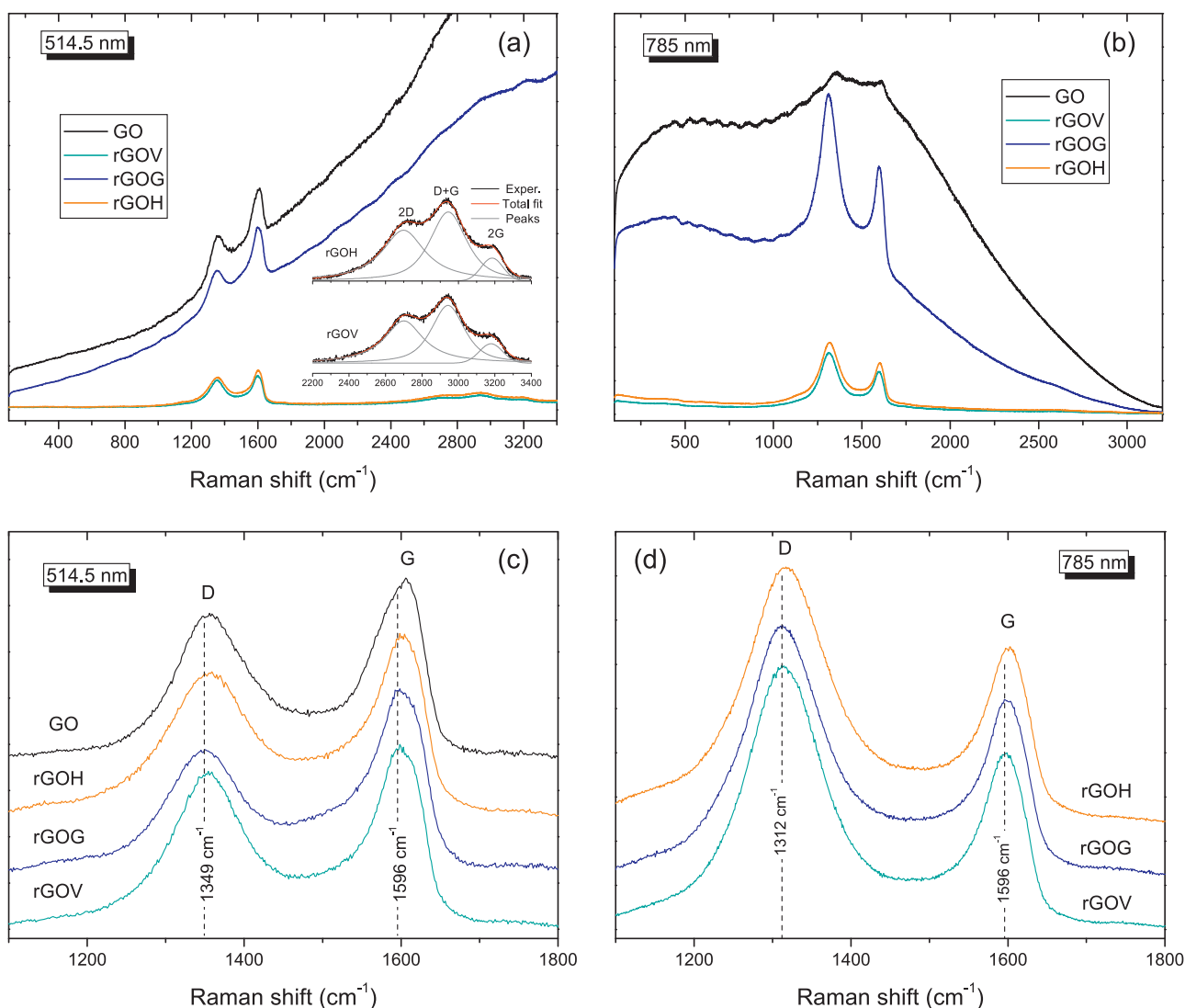


Fig. 4. Raman spectra of the rGO and GO samples at (a)–(c) 514.5 and (b)–(d) 785 nm. The inset in (a) shows the spectral deconvolution of the high frequency mode (2D, D + D' and 2G) for the rGOV and rGOH samples after background subtraction at 514.5 nm.

of epoxy, ether or peroxide groups) [12,61,62]. The band around 1612 cm^{-1} is assigned to physisorbed water.

After the reduction process, the removal of the oxygen-containing groups of GO is clearly reflected by the ATR–FTIR spectra. In comparison with GO, the samples reduced with different chemical agents showed a decrease in the intensity of all the absorption bands. This decrease was slightly more significant when reduction was carried with vitamin C and hydrazine, in comparison with glucose. The absorption bands at $3000\text{--}3500\text{ cm}^{-1}$ and 1350 cm^{-1} , related to hydroxyl groups, show that these groups were not completely removed from the GO surface. Besides, in general, one absorption band was observed to remain at $1560\text{--}1600\text{ cm}^{-1}$, which relates to the graphitic structure of graphene nanosheets [14,59]. The bands at 1720 cm^{-1} (C=O) and 1050 cm^{-1} (C–O) remained in the reduced materials indicating that a fraction of the oxygen groups persists after all the different chemical processes [49], in agreement with the XPS analysis (Fig. S1, Table 1).

3.5. Raman spectroscopy

In Fig. 4 the Raman spectra of the rGO samples is compared with the pristine GO at 514.5 and 785 nm laser excitations, respectively. All samples exhibited the graphitic G band arising from the bond

stretching of sp^2 carbon atoms and the dispersive, defect-activated D band together with the high frequency modes, including the 2D band, the defect activated combination mode (D + D') and the 2G overtone that could be best resolved at 514.5 nm, as shown in the inset of Fig. 4a. There is an intense low-energy tail that drifts away the base line of rGOG, which is identified with a rather broad photoluminescence (PL) emission due to the background of the Raman spectra excited at 514.5 nm. On the other hand, this PL background was considerably reduced for both the rGOV and rGOH samples. The intense PL is similar to that of bare GO [25,63,64], whose broad emission spanning the visible to the NIR spectral range has been related to the size dependent radiative electron–hole recombination of sp^2 clusters in the sp^3 C–O matrix of GO [65].

Analysis of the Raman spectra in the range of $1100\text{--}1800\text{ cm}^{-1}$ (Figs. 4c and d for 514.5 and 785 nm, respectively), showed that the G band attained a broad, asymmetric shape for all the rGO samples, characteristic of disordered graphite rather than pristine GO [66], which confirmed the efficient reduction of GO. Specifically, significant spectral weight of the G band shifted to the lower frequency side, as expected from the merging of the tangential G mode with the higher frequency defect activated D' band ($\sim 1620\text{ cm}^{-1}$) for disordered graphitic materials [67,68]. This line shape is distinctively different from that of pristine GO, where spectral weight is

oppositely shifted to the high frequency side, possibly due to the diverse contributions of alternating single-double carbon bonds within GO [66]. This effect was most prominent at 514.5 nm, where the PL background and the D' band intensity were relatively reduced allowing direct comparison between the rGO and pristine GO samples, as shown in Fig. 4c. Furthermore, the apparent position of the G band shifted from 1596 cm^{-1} for rGOG and rGOV to $\sim 1600 \text{ cm}^{-1}$ for rGOH, compared to the bare GO ($\sim 1605 \text{ cm}^{-1}$) (Fig. 4c-d). This behaviour indicates a similar trend in the reduction efficiency for the rGO samples complying favourably with the XPS analysis, i.e. $\text{rGOV} \sim \text{rGOG} > \text{rGOH}$, as GO reduction tends to restore the G band position to the corresponding value for crystalline graphite, i.e. 1582 cm^{-1} [69,70].

Besides the frequency shift of the G band, appreciable variations were observed in the relative intensities of the D bands for the different rGO samples, which may also reflect the different degree of GO reduction. However, quantitative analysis of the rGO Raman spectra in the frequency range $1100\text{--}1800 \text{ cm}^{-1}$ by fitting to three independent Raman bands (G, D and D') was rather approximate. Accurate spectral analysis could be obtained by including two additional broad bands, D₃ ($\sim 1500 \text{ cm}^{-1}$) and D₄ ($\sim 1200 \text{ cm}^{-1}$), associated with the presence of amorphous carbon and disordered graphitic material, respectively [71]. On the other hand, no satisfactory fit could be obtained in the pristine GO Raman spectrum by this procedure, indicative of the marked effects on its vibrational characteristics due to the extensive coverage by oxygen groups. Figs. S2 a-b, c-d and e-f display the corresponding spectral fits at 514.5 and 785 nm for rGOV, rGOG and rGOH, respectively, and Table 2 shows the obtained values for the Raman intensity ratios of the D, D₃ and D₄ bands (I_D/I_G , I_{D_3}/I_G and I_{D_4}/I_G) relative to the G mode for the rGO samples, calculated from the areas of the corresponding Raman bands, at 514.5 and 785 nm, respectively.

As seen in Table 2, rGOG presented the lowest I_D/I_G values followed by rGOV and rGOH, consistently with the shift of the G band position, suggesting that it contained the lowest amount of defects. On the other hand, rGOG exhibited the highest I_{D_3}/I_G ratio, implying the concomitant generation of appreciable amounts of amorphous carbon and/or remnants from glucose and even GO. The presence of carbonaceous remnants might also justify the high PL of the rGOG sample, in accordance with its lower thermal stability deduced from the TGA analysis.

3.6. Temperature programmed desorption (TPD)

TPD enables us to calculate the amounts of different types of oxygenated groups, which evolve as CO and CO₂. The TPD profiles for CO₂ and CO are shown in Figs. 5a-b respectively. Table 3 shows the total amounts of both CO₂ and CO, the respective oxygen content as well as the pH_{PZC} values for GO and the reduced materials.

The oxygen contents evolved during the TPD experiments follow the order (Table 3): GO (23.6 wt.%) > rGOH (6.1 wt.%) \sim rGOV (6.0 wt.%) > rGOG (5.8 wt.%) indicating a similar trend in the reduction efficiency for the rGO samples using the different reducing agents, in agreement with the results of Raman spectroscopy. Analysis of the surface by XPS showed higher oxygen contents (Table 1) than those obtained by TPD (Table 3), indicating that the oxygenated groups are mainly formed on the external surface of the graphene based material [72].

The high oxygen content and larger CO₂ and CO evolution (Figs. 5a-b respectively) detected for the GO sample correspond to the presence of a larger amount of oxygenated groups in comparison with the rGO samples (respectively, 5305 and $4156 \mu\text{mol g}^{-1}$ for GO, 957 and $1872 \mu\text{mol g}^{-1}$ for rGOH, 1215 and $1328 \mu\text{mol g}^{-1}$ for rGOV, and 1056 and $1517 \mu\text{mol g}^{-1}$ for rGOG), as also concluded from XPS (Fig. S1) and ATR-FTIR (Fig. 3) analyses. In general, as the

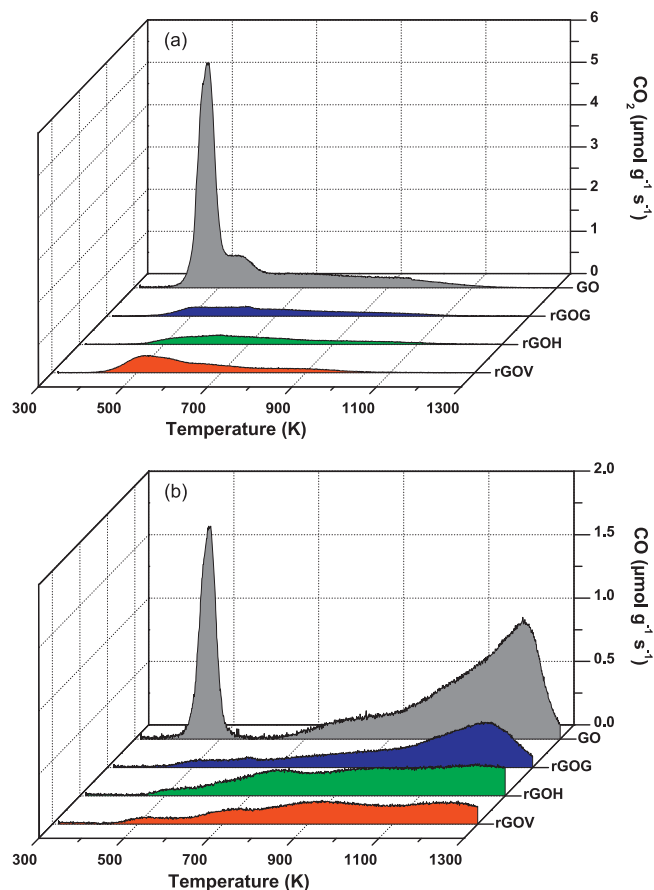


Fig. 5. TPD profiles for GO and reduced samples: (a) CO₂ and (b) CO release.

oxygen content decreases, the pH_{PZC} increases, indicating that the carbon surface becomes less acidic (Table 3).

In order to determine the amounts of each type of surface groups, deconvolution of both CO₂ and CO TPD signals was carried out (Figs. S3 a-b, c-d, e-f and g-h for GO, rGOH, rGOV and rGOG, respectively). The results obtained from the deconvolution of the TPD spectra are summarized in Tables 4 and 5 for CO₂ and CO, respectively. The thermal stability of oxygenated functional groups depends on the type of group and on the surroundings to which they are bounded. The deconvolution methodology was applied considering the temperatures at which the different groups evolved as CO₂ and CO upon heating as well as some assumptions according to the methodology reported in literature [73,74].

The deconvolution of CO₂ spectra for GO suggests the presence of five peaks. Peak 1 (E&H), at low temperatures ($\sim 471 \text{ K}$) has been ascribed to epoxy and hydroxyl groups located in basal plane sites, as also established from the XPS results (Table 1). These groups are expected to be released only as CO, and at higher temperatures; however, due to their high density in GO, the release as CO₂ is facilitated [33]. The low temperature associated with this peak has been already described for GO in literature [51,75]. Peak 2 ($\sim 544 \text{ K}$) and peak 3 ($\sim 629 \text{ K}$) were, respectively, assigned to strongly acidic carboxylic groups (SA) and weakly acidic carboxylic groups (WA). Peak 4 ($\sim 761 \text{ K}$) corresponds to anhydride groups (CA_n), which decompose by releasing one CO₂ and one CO molecule, and a final peak at $\sim 914 \text{ K}$ is associated with lactones (Lac).

Regarding the CO-TPD spectra of GO, peak 1 ($\sim 471 \text{ K}$) is assigned to the basal plane epoxy and hydroxyl groups (E&H), also released as CO₂. Peak 2 ($\sim 840 \text{ K}$) corresponds to carboxylic anhydrides (CA_n) appearing at a different temperature than that observed for the CO₂ spectra. This effect was attributed to either the re-adsorption

Table 2Integrated intensity ratios of the D, D₃ and D₄ bands for the rGO samples.

	I_D/I_G		I_{D_3}/I_G		I_{D_4}/I_G	
	514.5 nm	785 nm	514.5 nm	785 nm	514.5 nm	785 nm
rGOH	2.50	4.58	0.51	0.42	0.09	0.14
rGOV	2.16	4.26	0.42	0.37	0.07	0.03
rGOG	1.85	4.00	0.56	0.53	0.02	0.01

Table 3Total amounts of CO₂ and CO released by TPD, O₂ content, CO/CO₂ ratio, and pH at the point of zero charge (pH_{PZC}).

Sample	CO ₂ (μmol g ⁻¹)	CO (μmol g ⁻¹)	O (%)	CO/CO ₂	pH _{PZC}
GO	5305	4156	23.6	0.8	2.8
rGOH	957	1872	6.1	2.0	5.5
rGOV	1215	1328	6.0	1.1	5.1
rGOG	1056	1517	5.8	1.5	5.2

of CO on carbon sites vacated after decomposition at lower temperatures of carboxyl groups or the stronger adsorption of CO on the carbon surface, as previously observed in oxidized samples [76]. In this case, the temperature difference between CO₂ and CO release can be as high as 100 K. Peak 3 (~990 K) corresponds to phenols/ether groups (*Ph*), and at higher temperature decomposed carbonyl/quinone groups (*CQ*) located in energetically different sites (peak 4 and 5, respectively, at ~1139 and ~1224 K) [73,74,76].

These results are in agreement with those obtained by ATR–FTIR (Fig. 3) and XPS (Figs. S1 a–b) showing the complex chemical composition of GO that contains mainly epoxy and hydroxyl groups on the basal planes as well as minor content of carbonyls, carboxyls, ethers, quinones, lactones, and phenols attached at vacancy and edge sites [75,77,78].

Regarding the rGO samples, the peak at low temperature (~471 K) was not observed while the other peaks at higher temperatures were partially reduced in both CO₂–TPD and CO–TPD spectra (Figs. 5a–b). These results are in agreement with previous studies of chemical reduction [10,51] involving mainly epoxy and hydroxyl groups located on the basal planes of GO, as they are less stable.

The deconvolution of the CO₂–TPD profiles in the rGO samples were assigned to both strongly (500–550 K/*SA*) and weakly (600–615 K/*WA*) acidic carboxylic groups, carboxylic anhydrides (660–720 K/*CAn*) and lactones (870–980 K/*Lac*) whereas for CO–TPD profiles the contributions were assigned to carboxylic anhydrides (710–790 K/*CAn*), phenols (900–950 K/*Ph*) and carbonyl/quinone groups (1060–1300 K/*CQ*), as shown in Tables 4 and 5. In addition, a peak in the CO spectrum was observed at the same temperatures where the carboxylic acids evolve in the CO₂ spectrum (510–530 K), labelled as *CAC*; however, this peak is not yet fully understood in literature.

It can be observed that the amount of oxygen functionalities in the reduced samples is determined by the reducing agent used

(Tables 4 and 5). In general, chemical reduction with both hydrazine and glucose (respectively, samples rGOH and rGOG) can remove larger amounts of carboxylic acids that reduction performed with vitamin C (150, and 179 μmol g⁻¹, 185 and 227 μmol g⁻¹, or 391 and 310 μmol g⁻¹ for strong and weak carboxylic acids of rGOH, rGOG or rGOV, respectively). However, higher removal of carboxylic anhydrides was obtained in rGOV (422, 416 and 264 μmol g⁻¹ for rGOH and rGOG and rGOV, respectively), while larger amounts of phenol groups were removed in GO reduced with glucose, rGOG (530, 346 and 143 μmol g⁻¹ for rGOH, rGOV and rGOG, respectively). For the remaining oxygenated groups, the removal was comparable, regardless of the reducing agent (Tables 4 and 5). Therefore, the chemical reducing treatments also lead to the partial removal of the more stable oxygenated groups as phenol, carbonyl, and carboxyl groups. This is not in agreement with previous reports, where chemical reduction cannot remove these types of oxygen groups [79].

Determination of the exact mechanism underlying the chemical reduction of GO is still a challenging task. However, the reduction of GO by hydrazine has been addressed in a few papers using molecular simulations [2,10]. In these studies, several reduction pathways for de-epoxidation by hydrazine were devised. All routes start from the ring-opening of epoxy groups and formation of hydroxyl groups on the original sites. These groups are not stable even at moderate temperatures, and can be removed or migrate to the edges of aromatic domains, restoring the conjugated structure. Gao et al. [10] also have reported that the oxygen functionalities of GO can be divided according to their location on the GO structure, as shown in Fig. S4, i.e. epoxy and hydroxyl groups located at the interior of an aromatic domain of GO (sites 1 and 2, respectively) and at the edge of an aromatic domain (sites 1' and 2', respectively, in the case of 2' the reactivity could be more close to that of phenol), carboxyl at the edge of an aromatic domain (site 3) and carbonyl at the edge of an

Table 4Results obtained from the deconvolution of CO₂ TPD spectra for GO and reduced samples. *T_M*, *W* and *A* correspond to the temperature, width at half-height and area of the peak, respectively.

Sample	Epoxy and hydroxyl (<i>EE&H</i>)			Carboxylic acid (<i>SA & WA</i>)			Carboxylic anhydride (<i>CAn</i>)			Lactone (<i>Lac</i>)		
	<i>T_M</i> (K)	<i>W</i> (K)	<i>A</i> (μmol g ⁻¹)	<i>T_M</i> (K)	<i>W</i> (K)	<i>A</i> (μmol g ⁻¹)	<i>T_M</i> (K)	<i>W</i> (K)	<i>A</i> (μmol g ⁻¹)	<i>T_M</i> (K)	<i>W</i> (K)	<i>A</i> (μmol g ⁻¹)
GO	471	37	3005	544 ^a 629 ^b	59 ^a 150 ^b	568 ^a 599 ^b	761	191	463	914	191	671
rGOH	n.d.	n.d.	n.d.	543 ^a 612 ^b	116 ^a 153 ^b	150 ^a 179 ^b	716	212	422	977	212	206
rGOV	n.d.	n.d.	n.d.	514 ^a 603 ^b	92 ^a 156 ^b	391 ^a 310 ^b	663	199	264	878	199	249
rGOG	n.d.	n.d.	n.d.	504 ^a 608 ^b	81 ^a 118 ^b	185 ^a 227 ^b	710	275	416	904	275	228

n.d.: not detected.

^a Strongly acidic carboxylic groups (*SA*).^b Weakly acidic carboxylic groups (*WA*).

Table 5
Results obtained from the deconvolution of CO TPD spectra for GO and reduced samples. T_M , W and A correspond to the temperature, width at half-height and area of the peak, respectively.

Sample	Epoxy and hydroxyl (E&H)			Carboxylic acid (C&C)			Carboxylic anhydride (C&A)			Phenol (Ph)			Carbonyl/quinone (CQ)		
	T_M (K)	W (K)	A ($\mu\text{mol g}^{-1}$)	T_M (K)	W (K)	A ($\mu\text{mol g}^{-1}$)	T_M (K)	W (K)	A ($\mu\text{mol g}^{-1}$)	T_M (K)	W (K)	A ($\mu\text{mol g}^{-1}$)	T_M (K)	W (K)	A ($\mu\text{mol g}^{-1}$)
GO	471	36	1011	n.d.	n.d.	n.d.	840	191	463	990	145	437	1139	145	1511
rGOH	n.d.	n.d.	n.d.	511	81	31	720	212	422	954	250	530	1224*	73*	690*
rGOV	n.d.	n.d.	n.d.	512	79	45	710	199	264	906	187	346	1307*	243*	602*
rGOG	n.d.	n.d.	n.d.	525	156	72	789	275	416	955	167	143	1062	187	239
													1240*	205*	435*
													1121	167	590
													1214*	106*	318*

n.d.: not detected.

* CQ located in different energetic sites.

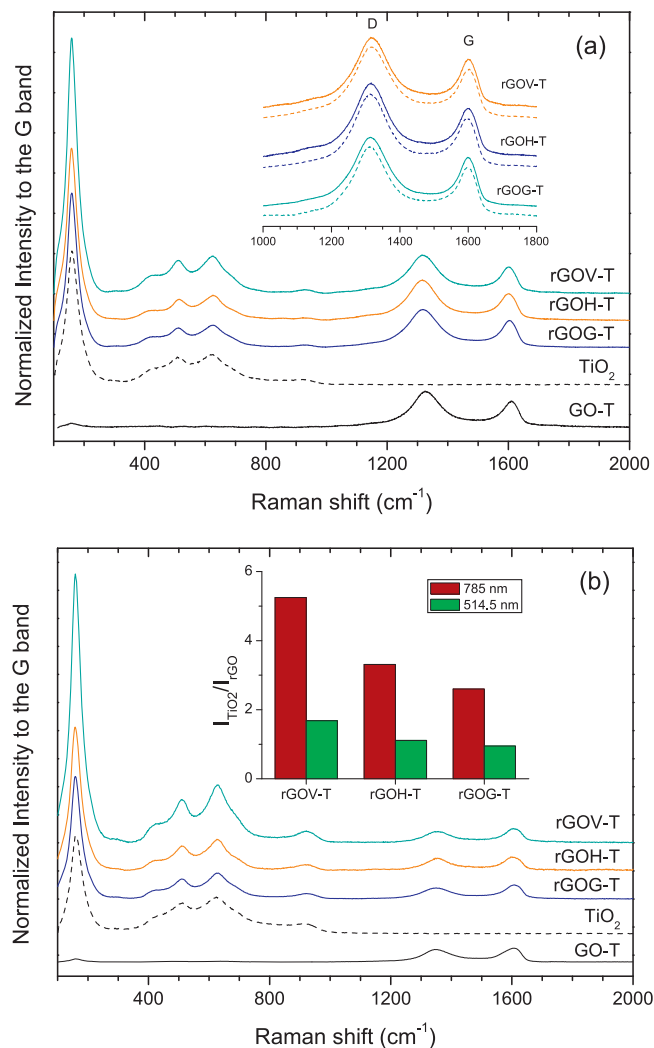


Fig. 6. Raman spectra of the rGO-T, GO-T and Bare-TiO₂ samples at (a) 785 and (b) 514.5 nm. The amplitude of the rGO- and GO-T Raman spectra has been normalized by that of the G band. The inset in (a) compares in detail the G and D bands of rGO-T with the corresponding spectrum of the bare rGO. The inset in (b) shows the intensity ratios $I_{\text{TiO}_2}/I_{\text{rGO}}$ for the different rGO-T composites at 514.5 and 785 nm.

aromatic domain (site 4). Solís-Fernández et al. [51] suggested that during thermal desorption the epoxy groups located at the edges of the aromatic domain could be transformed into more stable functionalities, i.e. epoxy groups into carbonyls and, on the other hand, ethers and hydroxyl groups into phenol groups. In the case of the reduced samples, it seems that both epoxy and hydroxyl species were eliminated by the reduction treatment and that the transformation of these groups to stable species during thermal desorption is not possible. This effect can explain the small amounts of both CO and CO₂ (corresponding to stable groups) released for the rGO samples above 773 K. Nevertheless, an exact model cannot be proposed for the GO structure, since the kind of functional groups and their distribution are determined both by the oxidation method and the starting material (graphite), which also affect the properties of GO.

3.7. Raman and diffuse reflectance UV-Vis spectroscopy (DRUV-Vis) for rGO-T and GO-T composites

The structural and optical properties of the graphene oxide-TiO₂ nanocomposites were subsequently investigated by Raman and diffuse reflectance UV-Vis spectroscopy. Fig. 6 summarizes the Raman spectra of GO- and rGO-T in comparison with bare TiO₂

at 514.5 and 785 nm, after subtraction of the photoluminescence background that was prominent only for the GO–T composite. The presence of both TiO_2 (vibration bands below 700 cm^{-1}) and GO (vibration bands higher than 1000 cm^{-1}) components was thus confirmed by their discrete Raman features for all composites with relative intensities that depended on the excitation energy. Specifically, the most intense Raman-active modes of the anatase TiO_2 phase were identified at 161 , 430 , 511 and 627 cm^{-1} for all the composites as well as the bare TiO_2 samples at both excitation wavelengths. Both the frequency and the width of these modes deviated significantly from those of bulk anatase, indicative of optical phonon confinement effects that lead to the broadening and shift of the Raman bands in nanostructured TiO_2 [80]. Using the peak position (161 cm^{-1}) and full-width at half-maximum-FWHM (42 cm^{-1}) of the most intense anatase Raman mode and the predictions of the phonon confinement model [81], we estimate the size of the anatase TiO_2 nanocrystallites deposited on the GO sheets by LPD to be $\sim 3\text{ nm}$, slightly smaller than that derived for the corresponding thermally reduced GO–T analogues [25].

The presence of rGO and GO in the composite materials was similarly identified by the characteristic D and G bands, whose intensity was appreciably enhanced over those of TiO_2 at 785 nm , indicative of a different dependence of the Raman cross section on the excitation laser energy for TiO_2 and GO. No appreciable variation (shift and/or broadening) of the G and D bands could be traced for the rGO–T composites compared to the bare rGO samples (inset of Fig. 6a), similar to the constant spectral characteristics of anatase Raman bands. A relative weak coupling can be accordingly inferred between the rGO and TiO_2 components that retain their structural integrity with no significant distortion upon binding in the rGO–T composites, independently of the differences in rGO reduction efficiency. However, the relative intensity of the anatase Raman modes with respect to those of rGO (G and D bands) varied considerably for the rGO–T samples (Fig. 6), despite their identical loading, as evidenced by the variation of the intensity ratio $I_{\text{TiO}_2}/I_{\text{rGO}}$ calculated by the integrated area of the low frequency E_g anatase mode to the corresponding area of the G and D rGO bands (inset of Fig. 6b). The latter ratio decreased consistently for both excitation wavelengths following the order of $\text{rGOV} > \text{rGOH} > \text{rGOG}$. This effect points to a different TiO_2 loading of the rGO–T composites, which could be related to the different degree of rGO reduction efficiency and the concomitant differences in the content of oxygenated groups that serve as anchoring sites for the TiO_2 nanoparticles.

On the other hand, a relatively stronger interfacial coupling may be inferred for the GO–T composite, where binding with TiO_2 resulted in the decrease of the photoluminescence background that obstructed the detection of the G and D bands for the pristine GO at 785 nm (Fig. 4b). In that case, assuming that the GO and rGO present similar Raman scattering efficiencies, the $I_{\text{TiO}_2}/I_{\text{rGO}}$ ratio was markedly lower (ca. 50-fold decrease) than those of the rGO–T composites, though comparable to those of the thermally reduced GO–T composites, where optimal assembly and interfacial GO–T coupling was reported [25].

Fig. S5 shows the DRUV–Vis spectra, expressed in terms of Kubelka–Munk absorption units, for the graphene– TiO_2 composites as well as that of the benchmark P25 material. The composites prepared with GO and rGO samples (regardless the method used) induce an absorption increase in the visible region. For the determination of band gaps, the transformed Kubelka–Munk function was plotted as a function of the energy of light as shown in Fig. S5 inset. The band gap values were estimated as ca. 2.9, 3.0, 3.0, 3.1 and 3.2 eV for rGOH–T, rGOV–T, GO–T, rGOG–T and P25, respectively. In all cases, narrower band gaps were obtained for the composites in comparison to P25, which can be related to the formation of Ti–O–C bonds between TiO_2 and graphene materials [15,82]. Among these samples, the degree of band gap narrowing was the highest for the

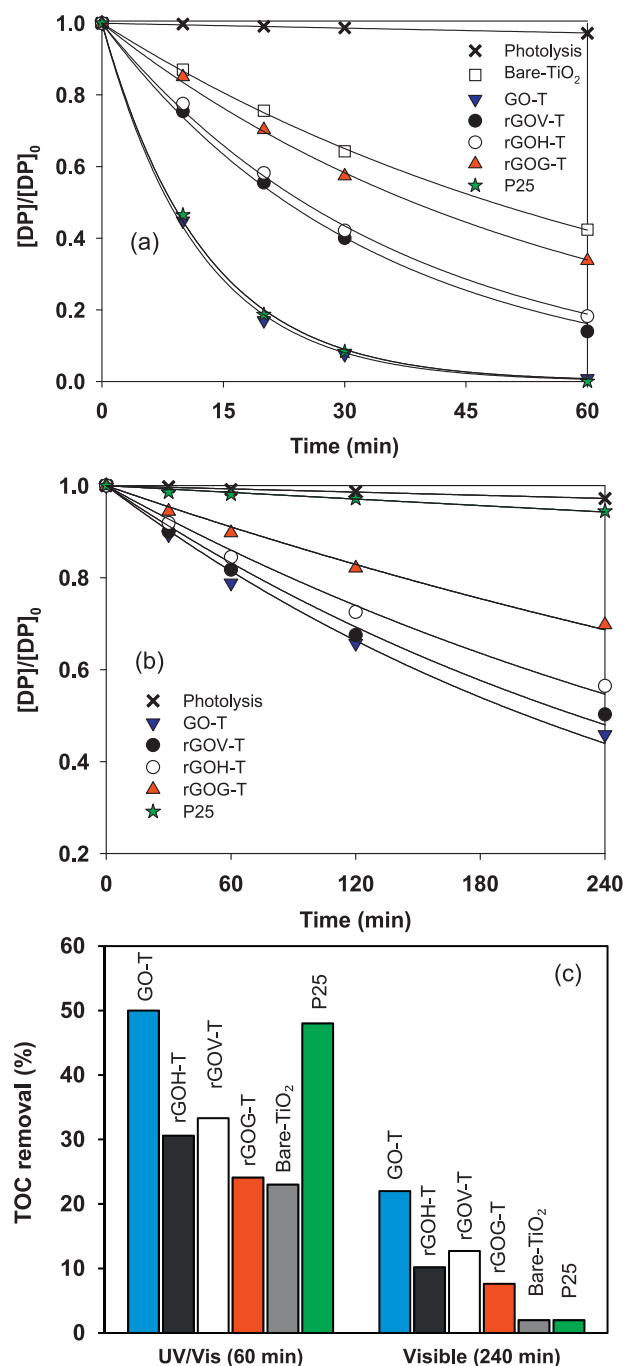


Fig. 7. Photocatalytic degradation of DP (100 mg L^{-1}) for P25, Bare- TiO_2 , GO–T, rGOV–T, rGOH–T and rGOG–T composites under (a) near-UV/Vis, and (b) visible light irradiation. (c) Total organic carbon (TOC) removal for the prepared catalysts and P25 under near-UV/Vis and visible light irradiation. Catalyst load = 1.0 g L^{-1} . Curves represent the fitting of the pseudo-first order equation to the experimental data.

rGOH–T composites, suggesting a relatively stronger interaction between TiO_2 and rGOH.

3.8. Photocatalytic experiments

In order to study the effect of the partial removal of oxygenated groups in GO on the photocatalytic performance of TiO_2 , a series of comparative tests were conducted for the degradation of DP under near-UV/Vis (Fig. 7a) and visible light irradiation (Fig. 7b) with bare TiO_2 (Bare- TiO_2) and with the composites obtained with GO (sample GO–T) and rGO (samples rGOH–T, rGOV–T and

Table 6
Pseudo first-order kinetic rate constant (k), respective coefficient of variation expressed as a percentage (k_{cv}) and regression coefficient (r^2) of DP degradation under near-UV/Vis and visible light irradiation.

	near-UV/Vis (60 min)			Visible (240 min)		
	k (10^{-3} min^{-1})	$k_{cv}(\%)$	r^2	k (10^{-3} min^{-1})	$k_{cv}(\%)$	r^2
GO-T	83.9 ± 1.9	2.3	0.991	3.4 ± 0.1	3.4	0.993
rGOH-T	27.8 ± 0.1	2.0	0.998	2.5 ± 0.1	3.4	0.992
rGOV-T	30.4 ± 0.7	2.4	0.998	3.1 ± 0.1	3.7	0.992
rGOG-T	18.1 ± 0.3	1.6	0.998	1.6 ± 0.1	3.3	0.992
Bare-TiO ₂	14.3 ± 0.2	1.0	0.9994	0.22 ± 0.05	7.0	0.995
P25	80.3 ± 1.8	2.3	0.9991	0.25 ± 0.05	9.6	0.998
Photolysis	0.45 ± 0.01	4.1	0.986	0.17 ± 0.06	3.7	0.98

rGOG-T) as well as with the P25 photocatalyst. The kinetic parameters were obtained by non-linear regression and the results are shown in Table 6. It can be seen that DP was very stable under UV/Vis and visible light irradiation without the presence of a photocatalyst ($k = 0.45 \times 10^{-3} \text{ min}^{-1}$ and $k = 0.17 \times 10^{-3} \text{ min}^{-1}$, respectively).

The results indicate that all the composites exhibited significantly higher rates for DP conversion (83.9×10^{-3} , 27.8×10^{-3} , 30.4×10^{-3} and $18.1 \times 10^{-3} \text{ min}^{-1}$ for GO-T, rGOH-T, rGOV-T and rGOG-T, respectively) than that observed for Bare-TiO₂ ($14.3 \times 10^{-3} \text{ min}^{-1}$) under near-UV/Vis (Table 6). This demonstrates that the presence of graphene derivatives can enhance the photocatalytic performance of TiO₂ under UV-Vis irradiation by accelerating the transfer of photo-generated electrons and suppressing charge carrier recombination [15].

The photocatalytic efficiency of the tested materials under near-UV/Vis irradiation followed the sequence GO-T ~ P25 > rGOV-T ~ rGOH-T > rGOG-T > TiO₂ (Fig. 7a and Table 6). The photocatalytic activity of the rGO-T composites correlated favourably with the differences in the TiO₂/rGO loadings derived from the Raman analysis (Fig. 6), indicating that the variation in the nature of the oxygenated groups of the rGO sheets is crucial for the loading of TiO₂ nanoparticles on rGO and, consequently, for their photocatalytic performance. In particular, among the rGO-T composites, rGOV-T was the most effective catalyst for DP degradation under near UV-Vis and visible irradiation (see below). This activity may be related with the larger amount of carboxylic acid groups in the surface of the material, as reported by Rivera-Utrilla et al. [83] when using an integrated UV/TiO₂/activated carbon system for the degradation of pesticides.

On the other hand, GO-T presented higher efficiency for DP degradation (comparable to that of P25) in comparison with the rGO-T composites, confirming that the photocatalytic activity of the composites is drastically influenced by the chemical reduction processes. This effect can be rationalized by the removal of the oxygenated surface groups from GO during the reducing processes, since these groups mediate the efficient and uniform assembly of the TiO₂ nanoparticles on the graphene oxide sheets [25]. Their removal is accordingly expected to partially dismantle the composite structure and disrupt the binding and charge transfer between GO and TiO₂, and eventually moderate the composite's photocatalytic efficiency. Stankovich et al. [2] reported that rGO dispersions also tend to aggregate in aqueous solutions because of the loss of oxygen-containing surface groups, resulting in the loss of surface area. In our case, the apparent surface area (S_{BET}) determined for the composites was systematically lower for the rGO-T composites than that obtained for the GO-T composite (i.e. S_{BET} of 136, 79, 40 and $28 \text{ m}^2 \text{ g}^{-1}$ for GO-T, rGOH-T, rGOV-T and rGOG-T, respectively). The rich GO surface chemistry should be then responsible not only for the good assembly of the TiO₂ particles on the GO sheets but also for their high dispersion in the solution during the preparation of the composites, giving composites with higher surface area.

Regarding visible light illumination, Fig. 7b and Table 6 present the results obtained for DP degradation with all catalysts for a reaction time of 240 min. The pseudo-first order rate constants for DP degradation under visible light illumination followed the trend: GO-T ($3.4 \times 10^{-3} \text{ min}^{-1}$) > rGOV-T ($3.1 \times 10^{-3} \text{ min}^{-1}$) > rGOH-T ($2.5 \times 10^{-3} \text{ min}^{-1}$) > rGOG-T ($1.6 \times 10^{-3} \text{ min}^{-1}$) > P25 ($0.25 \times 10^{-3} \text{ min}^{-1}$) ~ Bare-TiO₂ ($0.22 \times 10^{-3} \text{ min}^{-1}$), indicating that both Bare-TiO₂ and P25 are practically inactive under visible light conditions with similar rate to that obtained in the photolysis experiments ($0.17 \times 10^{-3} \text{ min}^{-1}$). On the other hand, the composites prepared with either GO or rGO were highly efficient in the DP degradation under visible illumination ($\lambda > 430 \text{ nm}$) providing firm evidence for the beneficial effect of combining graphene derivatives with TiO₂ for the photocatalytic degradation of water pollutants under visible light illumination. The observed enhancement of the photocatalytic activity in the composites could be in principle accounted by the interfacial charge transfer process from GO (or rGO) to TiO₂ that can effectively inhibit electron-hole recombination [25].

The TOC removal was also determined at the end of the experiments for the different photocatalysts under both near-UV/Vis (60 min) and visible light (240 min) illumination. In general, the determined mineralization showed a trend quite similar to that observed for DP conversion; i.e. GO-T, rGOH-T, rGOV-T, rGOG-T, Bare-TiO₂ and P25 led to TOC reductions of 50%, 31%, 33%, 24%, 23% and 48%, respectively, under near-UV/Vis light, and 22%, 10%, 13%, 8%, 2% and 2%, respectively, under visible light illumination. Therefore, GO-T presented not only the highest photocatalytic activity for DP degradation, but also the highest mineralization in comparison to all other materials tested under near-UV-Vis and visible light.

Graphene based-TiO₂ composites prepared with GO or rGO have shown high photocatalytic activity for the degradation of Orange II dye under UV and visible light irradiation [84]. However, we have found a different behaviour in the present work. The lower photocatalytic activity observed for the composites containing rGO (rGO-T), in comparison with that prepared with GO (GO-T), could be due to the very low amount of oxygenated surface groups that leads to a weak interaction between TiO₂ and rGO during the preparation method employed. The affinity of surface hydroxyl groups on TiO₂ surface to undergo charge transfer interaction with carboxylic acid functional groups on GO is reported in literature [5]. These effects can be responsible for the optimal assembly and interfacial coupling between GO sheets and TiO₂ nanoparticles during the preparation of the composite (consisting of GO platelets embedded into TiO₂), as well as for the higher photocatalytic performance of the GO-T composite.

4. Conclusions

Chemically reduced graphene oxide was prepared using three reducing agents, i.e. vitamin C, glucose and hydrazine. The diverse evolution of oxygenated groups on the chemically reduced GO's,

comprising mainly hydroxyl, epoxy, carbonyl, lactones and carboxyl groups, was systematically evaluated by XPS and TPD analyses complemented by thermogravimetric data together with ATR-FTIR and Raman spectroscopy. The most labile oxygen functional groups were identified as epoxy and hydroxyl groups located on basal planes of GO that were eliminated during the reduction process, whereas only partial reduction of the most stable groups located at the edges (e.g. carbonyl and carboxyl groups) was observed. Different graphene-TiO₂ composites were prepared with the pristine GO and rGO samples by the liquid phase deposition method. High photocatalytic performance for the degradation of diphenhydramine pollutant in aqueous solution, especially under visible light, was accordingly observed with all the composites, whose photocatalytic efficiencies were, however, distinctly influenced by the nature and amount of functional groups. The composite containing GO (GO-T) was the most active photocatalyst under near-UV/Vis and visible light irradiation, since the oxygenated groups mediate the efficient and uniform assembly of the TiO₂ nanoparticles on the graphene oxide sheets.

Acknowledgements

Financial support for this work was provided by projects PTDC/AAC-AMB/122312/2010 co-financed by FCT (Fundação para a Ciência e a Tecnologia) and FEDER (ERDF—European Regional Development Fund) through Programme COMPETE (FCOMP-01-0124-FEDER-019503). This work was also partially co-financed by FCT and FEDER through project PEst-C/EQB/LA0020/2013 (COMPETE), and by QREN, ON2 (North Portugal Regional Operational Programme) and FEDER through projects NORTE-07-0162-FEDER-000050, NORTE-07-0162-FEDER-000015 and NEPCAT (nr. 38900) in the National Strategic Reference Framework (NSRF). LMPM and SMT acknowledge financial support from FCT grants SFRH/BPD/88964/2012 and SFRH/BPD/74239/2010, respectively. AMTS acknowledges the FCT Investigator 2013 Programme (IF/01501/2013), with financing from the European Social Fund and the Human Potential Operational Programme. Technical assistance by Dr Carlos Sá and CEMUP team with XPS analysis is gratefully acknowledged.

Appendix A. Supplementary data

Supplementary data associated with this article can be found, in the online version, at <http://dx.doi.org/10.1016/j.apcatb.2014.04.024>.

References

- [1] S. Pei, H.-M. Cheng, *Carbon* 50 (2012) 3210–3228.
- [2] S. Stankovich, D.A. Dikin, R.D. Piner, K.A. Kohlhaas, A. Kleinhammes, Y. Jia, Y. Wu, S.T. Nguyen, R.S. Ruoff, *Carbon* 45 (2007) 1558–1565.
- [3] C. Botas, P. Álvarez, C. Blanco, R. Santamaría, M. Granda, M.D. Gutiérrez, F. Rodríguez-Reinoso, R. Menéndez, *Carbon* 52 (2013) 476–485.
- [4] Y. Shao, J. Wang, M. Engelhard, C. Wang, Y. Lin, *J. Mater. Chem.* 20 (2010) 743–748.
- [5] G. Williams, B. Seger, P.V. Kamat, *ACS Nano* 2 (2008) 1487–1491.
- [6] J.-H. Yun, Y.H. Ng, R.J. Wong, R. Amal, *ChemCatChem* 5 (2013) 3060–3067.
- [7] L. Huang, Y. Liu, L.-C. Ji, Y.-Q. Xie, T. Wang, W.-Z. Shi, *Carbon* 49 (2011) 2431–2436.
- [8] C.K. Chua, M. Pumera, *Chem. Soc. Rev.* 43 (2014) 291–312.
- [9] S. Park, J. An, J.R. Potts, A. Velamakanni, S. Murali, R.S. Ruoff, *Carbon* 49 (2011) 3019–3023.
- [10] X. Gao, J. Jang, S. Nagase, *J. Phys. Chem. C* 114 (2009) 832–842.
- [11] J. Gao, F. Liu, Y. Liu, N. Ma, Z. Wang, X. Zhang, *Chem. Mater.* 22 (2010) 2213–2218.
- [12] M.J. Fernández-Merino, L. Guardia, J.I. Paredes, S. Villar-Rodil, P. Solís-Fernández, A. Martín-Nez-Alonso, J.M.D. Tasco'n, *J. Phys. Chem. C* 114 (2010) 6426–6432.
- [13] C. Zhu, S. Guo, Y. Fang, S. Dong, *ACS Nano* 4 (2010) 2429–2437.
- [14] T.A. Pham, J.S. Kim, J.S. Kim, Y.T. Jeong, *Colloids Surf., A: Physicochem. Eng. Aspects* 384 (2011) 543–548.
- [15] W. Fan, Q. Lai, Q. Zhang, Y. Wang, *J. Phys. Chem. C* 115 (2011) 10694–10701.
- [16] A. Esfandiari, O. Akhavan, A. Irajizad, *J. Mater. Chem.* 21 (2011) 10907–10914.
- [17] F. Yavari, N. Koratkar, *J. Phys. Chem. Lett.* 3 (2012) 1746–1753.
- [18] S. Wu, Q. He, C. Tan, Y. Wang, H. Zhang, *Small* 9 (2013) 1160–1172.
- [19] Y. Chen, X. Zhang, D. Zhang, P. Yu, Y. Ma, *Carbon* 49 (2011) 573–580.
- [20] I.T. Kim, A. Magasinski, K. Jacob, G. Yushin, R. Tannenbaum, *Carbon* 52 (2013) 56–64.
- [21] Y. Wen, Y. Zhu, A. Langrock, A. Manivannan, S.H. Ehrman, C. Wang, *Small* 9 (2013) 2810–2816.
- [22] J. Song, Z. Yin, Z. Yang, P. Amaladas, S. Wu, J. Ye, Y. Zhao, W.-Q. Deng, H. Zhang, X.-W. Liu, *Chem.—Eur. J.* 17 (2011) 10832–10837.
- [23] Y.T. Liang, B.K. Vijayan, K.A. Gray, M.C. Hersam, *Nano Lett.* 11 (2011) 2865–2870.
- [24] J. Du, X. Lai, N. Yang, J. Zhai, D. Kisailus, F. Su, D. Wang, L. Jiang, *ACS Nano* 5 (2010) 590–596.
- [25] L.M. Pastrana-Martínez, S. Morales-Torres, V. Likodimos, J.L. Figueiredo, J.L. Faria, P. Falaras, A.M.T. Silva, *Appl. Catal., B: Environ.* 123–124 (2012) 241–256.
- [26] L.-L. Tan, S.-P. Chai, A.R. Mohamed, *ChemSusChem* 5 (2012) 1868–1882.
- [27] Q. Xiang, J. Yu, M. Jaroniec, *Chem. Soc. Rev.* 41 (2012) 782–796.
- [28] X. An, J.C. Yu, *RSC Adv.* 1 (2011) 1426–1434.
- [29] S. Morales-Torres, L.M. Pastrana-Martínez, J.L. Figueiredo, J.L. Faria, A.M.T. Silva, *Environ. Sci. Pollut. Res.* 19 (2012) 3676–3687.
- [30] W. Wang, J. Yu, Q. Xiang, B. Cheng, *Appl. Catal., B: Environ.* 119–120 (2012) 109–116.
- [31] Y. Zhang, J. Tian, H. Li, L. Wang, X. Qin, A.M. Asiri, A.O. Al-Youbi, X. Sun, *Langmuir* 28 (2012) 12893–12900.
- [32] J. Yu, J. Jin, B. Cheng, M. Jaroniec, *J. Mater. Chem. A* 2 (2014) 3407–3416.
- [33] S. Liu, Z. Chen, N. Zhang, Z.-R. Tang, Y.-J. Xu, *J. Phys. Chem. C* 117 (2013) 8251–8261.
- [34] X. Liu, L. Pan, T. Lv, G. Zhu, Z. Sun, C. Sun, *Chem. Commun.* 47 (2011) 11984–11986.
- [35] Y. Wang, J. Yu, W. Xiao, Q. Li, *J. Mater. Chem. A* 2 (2014) 3847–3855.
- [36] Q. Xiang, J. Yu, *J. Phys. Chem. Lett.* 4 (2013) 753–759.
- [37] J. Fan, S. Liu, J. Yu, *J. Mater. Chem.* 22 (2012) 17027–17036.
- [38] Q. Xiang, J. Yu, M. Jaroniec, *Nanoscale* 3 (2011) 3670–3678.
- [39] G. Jiang, Z. Lin, C. Chen, L. Zhu, Q. Chang, N. Wang, W. Wei, H. Tang, *Carbon* 49 (2011) 2693–2701.
- [40] I.A. Appavoo, J. Hu, Y. Huang, S.F.Y. Li, S.L. Ong, *Water Res.* 57 (2014) 270–279.
- [41] V. Maroga Mboula, V. Héquet, Y. André, L.M. Pastrana-Martínez, J.M. Doña-Rodríguez, A.M.T. Silva, P. Falaras, *Water Res.* 47 (2013) 3997–4005.
- [42] T. Fotiou, M.T. Triantis, T. Kaloudis, L.M. Pastrana-Martínez, V. Likodimos, P. Falaras, A.M.T. Silva, A. Hiskia, *Ind. Eng. Chem. Res.* 52 (2013) 13991–14000.
- [43] A.J. Ramirez, R.A. Brain, S. Usenko, M.A. Mottaleb, J.G. O'Donnell, L.L. Stahl, J.B. Wathen, B.D. Snyder, J.L. Pitt, P. Perez-Hurtado, L.L. Dobbins, B.W. Brooks, C.K. Chambliss, *Environ. Toxicol. Chem.* 28 (2009) 2587–2597.
- [44] C.A. Kinney, E.T. Furlong, S.L. Werner, J.D. Cahill, *Environ. Toxicol. Chem.* 25 (2006) 317–326.
- [45] W.S. Hummers, R.E. Offeman, *J. Am. Chem. Soc.* 80 (1958) 1339.
- [46] L.M. Pastrana-Martínez, S. Morales-Torres, S.K. Papageorgiou, F.K. Katsaros, G.E. Romanos, J.L. Figueiredo, J.L. Faria, P. Falaras, A.M.T. Silva, *Appl. Catal., B: Environ.* 142–143 (2013) 101–111.
- [47] S. Brunauer, P.H. Emmett, E. Teller, *J. Am. Chem. Soc.* 60 (1938) 309–319.
- [48] J.I. Paredes, S. Villar-Rodil, P. Solís-Fernández, A. Martín-Nez-Alonso, J.M.D. Tasco'n, *Langmuir* 25 (2009) 5957–5968.
- [49] D. Li, M.B. Muller, S. Gilje, R.B. Kaner, G.G. Wallace, *Nat. Nano* 3 (2008) 101–105.
- [50] J.I. Paredes, S. Villar-Rodil, A. Martín-Nez-Alonso, J.M.D. Tasco'n, *Langmuir* 24 (2008) 10560–10564.
- [51] P. Solís-Fernández, R. Rozada, J.I. Paredes, S. Villar-Rodil, M.J. Fernández-Merino, L. Guardia, A. Martín-Nez-Alonso, J.M.D. Tasco'n, *J. Alloys Compd.* 536 (Suppl. 1) (2012) S532–S537.
- [52] D. Luo, G. Zhang, J. Liu, X. Sun, *J. Phys. Chem. C* 115 (2011) 11327–11335.
- [53] D. Yang, A. Velamakanni, G. Bozoklu, S. Park, M. Stoller, R.D. Piner, S. Stankovich, I. Jung, D.A. Field, C.A. Ventrice Jr., R.S. Ruoff, *Carbon* 47 (2009) 145–152.
- [54] K. Erickson, R. Erni, Z. Lee, N. Alem, W. Gannett, A. Zettl, *Adv. Mater.* 22 (2010) 4467–4472.
- [55] A. Pulido, P. Concepcion, M. Boronat, C. Botas, P. Alvarez, R. Menendez, A. Corma, *J. Mater. Chem.* 22 (2012) 51–56.
- [56] D. Deng, X. Pan, L. Yu, Y. Cui, Y. Jiang, J. Qi, W.-X. Li, Q. Fu, X. Ma, Q. Xue, G. Sun, X. Bao, *Chem. Mater.* 23 (2011) 1188–1193.
- [57] C. Botas, P. Alvarez, C. Blanco, M.D. Gutierrez, P. Ares, R. Zamani, J. Arbiol, J.R. Morante, R. Menendez, *RSC Adv.* 2 (2012) 9643–9650.
- [58] D. Zhou, Q.-Y. Cheng, B.-H. Han, *Carbon* 49 (2011) 3920–3927.
- [59] J. Sun, X. Teng, J. Yang, H. Bi, *J. Mater. Sci.* 48 (2013) 8277–8286.
- [60] M. Acik, G. Lee, C. Mattevi, A. Pirkle, R.M. Wallace, M. Chhowalla, K. Cho, Y. Chabal, *J. Phys. Chem. C* 115 (2011) 19761–19781.
- [61] M. Zhang, S. Liu, X.M. Yin, Z.F. Du, Q.Y. Hao, D.N. Lei, Q.H. Li, T.H. Wang, *Chem.—Asian J.* 6 (2011) 1151–1154.
- [62] Y. Xu, H. Bai, G. Lu, C. Li, G. Shi, *J. Am. Chem. Soc.* 130 (2008) 5856–5857.
- [63] Z. Luo, P.M. Vora, E.J. Mele, A.T.C. Johnson, J.M. Kikkawa, *Appl. Phys. Lett.* 94 (2009) 111909–111911.
- [64] T.V. Cuong, V.H. Pham, Q.T. Tran, S.H. Hahn, J.S. Chung, E.W. Shin, E.J. Kim, *Mater. Lett.* 64 (2010) 399–401.
- [65] K.P. Loh, Q. Bao, G. Eda, M. Chhowalla, *Nat. Chem.* 2 (2010) 1015–1024.
- [66] K.N. Kudin, B. Ozbas, H.C. Schniepp, R.K. Prud'homme, I.A. Aksay, R. Car, *Nano Lett.* 8 (2007) 36–41.
- [67] R.J. Nemanich, S.A. Solin, *Phys. Rev. B: Condens. Matter* 20 (1979) 392–401.
- [68] T. Gokus, R.R. Nair, A. Bonetti, M. Böhm, A. Lombardo, K.S. Novoselov, A.K. Geim, A.C. Ferrari, A. Hartschuh, *ACS Nano* 3 (2009) 3963–3968.

- [69] M.A. Pimenta, G. Dresselhaus, M.S. Dresselhaus, L.G. Cancado, A. Jorio, R. Saito, *Phys. Chem. Chem. Phys.* 9 (2007) 1276–1290.
- [70] G.K. Ramesha, S. Sampath, *J. Phys. Chem. C* 113 (2009) 7985–7989.
- [71] A. Sadezky, H. Muckenhuber, H. Grothe, R. Niessner, U. Pöschl, *Carbon* 43 (2005) 1731–1742.
- [72] S. Morales-Torres, F.J. Maldonado-Hódar, A.F. Pérez-Cadenas, F. Carrasco-Marín, *J. Hazard. Mater.* 183 (2010) 814–822.
- [73] J.L. Figueiredo, M.F.R. Pereira, M.M.A. Freitas, J.J.M. Órfão, *Carbon* 37 (1999) 1379–1389.
- [74] J.L. Figueiredo, M.F.R. Pereira, M.M.A. Freitas, J.J.M. Órfão, *Ind. Eng. Chem. Res.* 46 (2007) 4110–4115.
- [75] A. Lerf, H. He, M. Forster, J. Klinowski, *J. Phys. Chem. B* 102 (1998) 4477–4482.
- [76] A.E. Aksoylu, M. Madalena, A. Freitas, M.F.R. Pereira, J.L. Figueiredo, *Carbon* 39 (2001) 175–185.
- [77] L.B. Casabianca, M.A. Shaibat, W.W. Cai, S. Park, R. Piner, R.S. Ruoff, Y. Ishii, *J. Am. Chem. Soc.* 132 (2010) 5672–5676.
- [78] W. Cai, R.D. Piner, F.J. Stadermann, S. Park, M.A. Shaibat, Y. Ishii, D. Yang, A. Velamakanni, S.J. An, M. Stoller, J. An, D. Chen, R.S. Ruoff, *Science* 321 (2008) 1815–1817.
- [79] M.C. Kim, G.S. Hwang, R.S. Ruoff, *J. Chem. Phys.* 131 (2009) 064704.
- [80] S. Kelly, F.H. Pollak, M. Tomkiewicz, *J. Phys. Chem. B* 101 (1997) 2730–2734.
- [81] A. Pottier, S. Cassaignon, C. Chaneac, F. Villain, E. Tronc, J.-P. Jolivet, *J. Mater. Chem.* 13 (2003) 877–882.
- [82] S. Morales-Torres, L.M. Pastrana-Martínez, J.L. Figueiredo, J.L. Faria, A.M.T. Silva, *Appl. Surf. Sci.* 275 (2013) 361–368.
- [83] J. Rivera-Utrilla, M. Sánchez-Polo, M.M. Abdel daïem, R. Ocampo-Pérez, *Appl. Catal., B: Environ.* 126 (2012) 100–107.
- [84] V. Stengl, J. Henych, P. Vomáčka, M. Slušná, *Photochem. Photobiol.* 89 (2013) 1038–1046.